Macromolecules

Article

Cite This: Macromolecules 2017, 50, 9674−9682

Tailoring Phase Transition in Poly(3-hexylselenophene) Thin Films and Correlating Their Crystalline Polymorphs with Charge Transport Properties for Organic Field-Effect Transistors

Yue Wang,[†] Huina Cui,[†] Mingjing Zhu,[†] Feng Qiu,[†] Juan Peng,*[,†] and Zhiqun Lin*[,‡]

[†]State Key Laboratory of Molecular Engineering of Polymers, Department of Macromolecular Science, Fudan University, Shanghai 200433, China

[‡]School of Materials Science and Engineering, Georgia Institute of Technology, Atlanta, Georgia 30332, United States

Supporting Information

ABSTRACT: Poly(3-hexylselenophene) (P3HS) carries attractive advantages over their close analogue poly(3-hexylthiophene) (P3HT), including a stronger intermolecular interaction, a better interchain charge hopping, and a narrower bandgap. However, P3HS is much less studied compared to P3HT. Herein, we report on intriguing reversible phase transition between two different crystalline polymorphs (i.e., form I and II) in P3HS thin films with different molecular weights enabled by alternating thermal and solvent vapor annealing. More importantly, the phase transition kinetics and mechanism as well as the associated changes on molecular packing structures were also scrutinized. The correlation between different P3HS crystalline polymorphs and the resulting field-effect mobilities was explored *for the first time*. Our study provides an insight into P3HS crystallization and phase transition, thus entailing the use of polyselenophene-based materials for a wide range of optoelectronic applications.

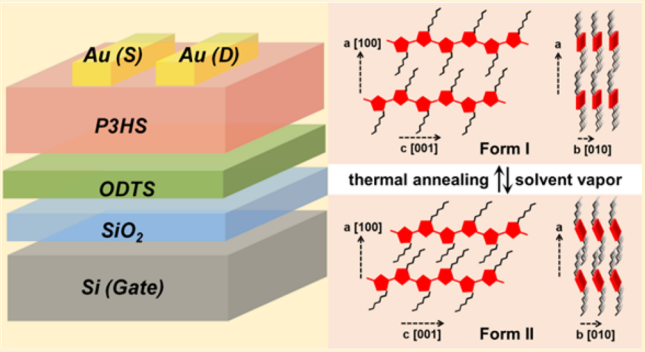

INTRODUCTION

Conjugated polymer-based organic field-effect transistors (OFETs) have garnered much interest due to their low cost, lightweight, flexibility, and solution processability.[1,2] Among various conjugated polymers, regioregular poly(3-alkylthiophene)s (P3ATs), particularly poly(3-hexylthiophene (P3HT), has been studied extensively.[3−7] Owing to a rigid conjugated backbone and the flexible alkyl side chains, P3ATs preferentially crystallize and self-assemble in an edge-on orientation manner with the alkyl side chains (*a*-axis) perpendicular to the substrate while for both the $\pi-\pi$ stacking (*b*-axis) of adjacent chain backbones and the backbone of a chain (*c*-axis) parallel to the substrate. Clearly, from the OFET device standpoint, such an edge-on orientation facilitates holes of P3ATs to hop from the source to the drain, thereby achieving high charge carrier mobility.

It is widely recognized that controlling the crystalline structure of conjugated polymers via tuning their molecular packing is the key to high performance optoelectronic devices. To date, the tuning of a set of intrinsic and extrinsic parameters such as regioregularity,[8,9] molecular weight,[10,11] solvent,[12,13] aging,[14] application of electric field,[15,16] thermal or solvent annealing,[17,18] etc., has been proven to be effective in controlling the crystalline structures of polythiophenes. These strategies may also be extended to polyselenophenes. It is important to note that compared to the heavily studied polythiophenes, their close analogues polyselenophenes are far less investigated due primarily to their high synthesis difficulty and relatively poor solubility.[19−24] By replacing sulfur atoms in the thiophene rings with the lower electronegative and more polarizable selenium atoms, the resulting polyselenophenes possess some advantageous attributes over polythiophenes, such as stronger intermolecular interaction, lower oxidation and reduction potential, better interchain charge transport, lower bandgap, etc.[24] A recent pioneering study on crystallization of poly(3-hexylselenophene) (P3HS) has demonstrated that there are different crystalline polymorphs, that is, form I and II with the interlayer spacings of 15.5 and 12.1 Å, respectively.[25] Because of the interdigitation of hexyl side chains, form II has a shorter interlayer spacing between the conjugated backbones than form I. Notably, there are comparatively few works on P3HS and its optical and electrical properties,[25−27] and the crystallization behavior remains largely less understood. More importantly, the relationship between different crystalline structures and charge transport properties in P3HS-based OFET has yet to be explored.

Herein, we report on reversible phase transition kinetics between two crystalline polymorphs (i.e., forms I and II) in

Received: October 2, 2017
Revised: November 12, 2017
Published: December 12, 2017

DOI: 10.1021/acs.macromol.7b02126
Macromolecules 2017, 50, 9674−9682

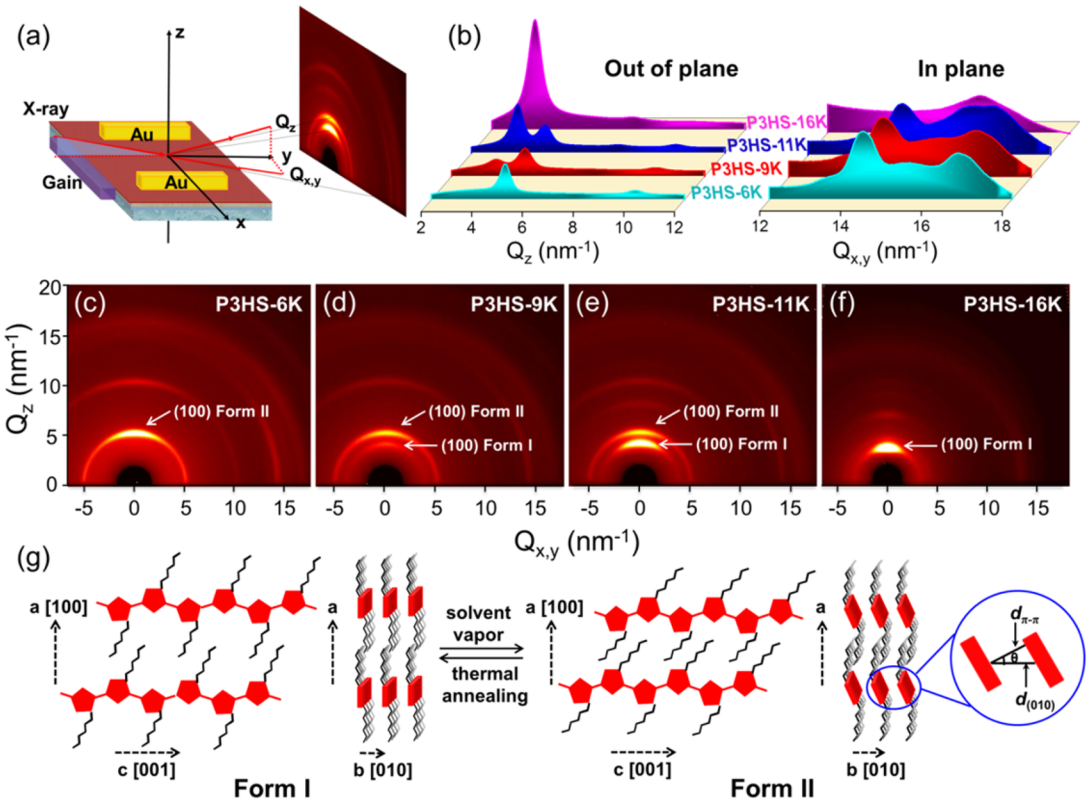

Figure 1. (a) Schematic illustration of the synchrotron GIXRD measurement for the P3HS film on a Si/SiO_2 substrate where the incidence angle of the synchrotron X-ray beam is 0.15°. (b) 1D GIXRD profiles reduced along the out-of-plane and in-plane directions from the corresponding 2D GIXRD images. (c–f) 2D GIXRD images of as-cast P3HS films with different molecular weights (6K, 9K, 11K, and 16K for panels c, d, e, and f, respectively). (g) Schematic representation of P3HS form I (left) and form II (right) polymorphs.

P3HS thin films of different molecular weights imparted by alternating the thermal and solvent vapor annealing processes and scrutinize the strong correlation between the crystalline polymorphs with the field-effect mobilities of P3HS. The emergence of form I and II of P3HS crystals was found to depend heavily on the molecular weights of P3HS and the modes of annealing (thermal vs solvent vapor). Pure form II existed in P3HS film at low molecular weight, while form I gradually dominated as the molecular weight increased. Quite interestingly, a reversible phase transition between form I and form II was observed in all the P3HS films, namely, form I to II upon solvent vapor annealing and form II to I via subsequent thermal annealing. It is noteworthy that such a phase transition is highly reversible and has not been previously investigated. The phase transition kinetics and mechanism as well as the associated changes on molecular packing structures were elaborated. Finally, the correlation between two different crystal forms of P3HS and the resulting field-effect mobilities was *for the first time* explored.

EXPERIMENTAL SECTION

Materials. The monomer 2,5-dibromo-3-hexylselenophene was synthesized according to the literature.[28] Isopropylmagnesium chloride (i-PrMgCl, 2.0 M in tetrahydrofuran), (1,3-bis(diphenylphosphino)-propane)dichloronickel(II) ($Ni(dppp)Cl_2$), and octadecyltrichlorosilane (ODTS) were purchased from Aldrich and used as received. Tetrahydrofuran (THF) was dried over sodium/benzophenone under an inert atmosphere and freshly distilled prior to use. The other reagents and solvents were purchased from Sinopharm Chemical Reagent Co., Ltd. (SRC). P3HS with different molecular weights was synthesized by a modified Grignard metathesis procedure.[29] Detailed synthetic procedures, further purification steps, polymer characterizations (GPC and ^1H NMR), and a summary of P3HS molecular weights, polydispersity index (PDI), and regioregularity (RR) are presented in the Supporting Information (Figures S1 and S2, Table S1).

Sample Preparation. Thin films for GIXRD, XRD, FTIR, and FESEM studies were prepared by solution-casting 5 mg/mL P3HS toluene solution onto precleaned silicon wafers or KBr substrates followed by solvent evaporation at ambient conditions. The as-cast films were thermally annealed on a hot plate placed in a glovebox filled with argon. For solvent vapor annealing, the samples were exposed to the saturated THF vapor in a closed vessel kept at room temperature for various amounts of time.

OFET Device Fabrication. In order to characterize the charge transport properties of P3HS films, OFET devices with bottom-gate top-contact geometry were fabricated. Highly n-doped silicon wafers with 200 nm SiO_2 layer were used as gate and insulator, respectively. Prior to spin-coating the P3HS 10 mg/mL toluene solution, the Si/SiO_2 substrates were rinsed with acetone, methanol, and isopropanol, followed by plasma treatment for 10 min, and then modified with ODTS. After thermal or solvent annealing of P3HS films, the source/drain electrodes were fabricated by evaporating a 30 nm gold onto the P3HS films through a shadow mask with a channel length and width of 30 and 300 μm, respectively.

Characterization. Grazing-incidence X-ray diffraction (GIXRD) experiments were carried out at the BL14B1 beamline of Shanghai Synchrotron Radiation Facility (SSRF), with a fixed wavelength of 1.24 Å. X-ray diffraction (XRD) was performed on a PANalytical X'Pert PRO X-ray diffractometer using Cu Kα radiation (λ = 1.541 Å) operating at 40 kV and 40 mA. Fourier transform infrared (FTIR) spectra were collected using a Nicolet 6700 spectrometer equipped with a hot stage. The sample was heated at a 2 °C/min from room temperature to 260 °C in a nitrogen atmosphere. During the heating process, FTIR spectra of the sample were recorded at a 10 °C interval

DOI: 10.1021/acs.macromol.7b02126
Macromolecules 2017, 50, 9674–9682

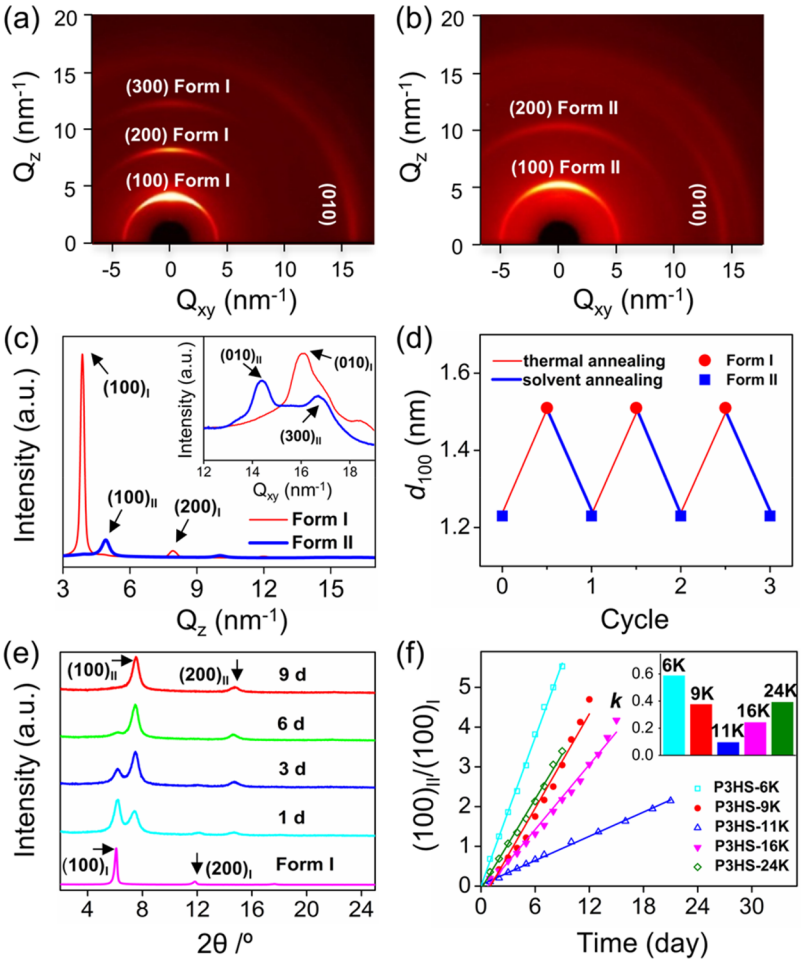

Figure 2. (a) 2D GIXRD image of the P3HS-6K film upon thermal annealing at 150 °C for 10 min, showing the (h00) diffraction planes of form I crystals. (b) Subsequent swelling of the P3HS film in (a) with THF vapor recovers the form II crystals. (c) 1D GIXRD profiles reduced along the out-of-plane and in-plane (inset) directions from (a) (form I) and (b) (form II). (d) Reversible d_{100} spacing changes of the P3HS-6K form I and form II films by repeated thermal annealing and THF vapor annealing, respectively. (e) XRD spectra showing the kinetic transformation process of P3HS-6K from form I to II crystals upon THF vapor annealing. The peak intensity in each curve of (e) was normalized. The (100) and (200) diffractions of form I and II crystals of P3HS are denoted $(100)_I$, $(200)_I$, $(100)_{II}$, and $(200)_{II}$. (f) The $(100)_{II}/(100)_I$ intensity ratio of P3HS films with different molecular weights as a function of THF vapor annealing time. The inset compares the slope k of different curves, showing that the P3HS-11K sample had the lowest form I to form II transition rate.

from 30 to 100 °C and from 180 to 260 °C and 5 °C interval from 100 to 180 °C. The spectra were obtained by coadding 64 scans at a 2 cm^{-1} resolution. Atomic force microscopy (AFM) was carried out on Multimode 8 AFM Nanoscope IV in the tapping mode. The electrical properties of the P3HS OFETs were measured using a Keithley 4200-SCS in an argon-filled glovebox.

RESULTS AND DISCUSSION

The molecular packing and crystal orientation of as-cast P3HS films with different molecular weights were thoroughly investigated by 2D synchrotron grazing-incidence X-ray diffraction (2D-GIXRD) (Figure 1). A schematic illustration of the synchrotron GIXRD measurement for P3HS films is depicted in Figure 1a. The 1D GIXRD profiles reduced along the out-of-plane (q_z) and in-plane ($q_{x,y}$) directions are presented in Figure 1b. Figures 1c–1f compare a family of (h00) diffraction planes along the out-of-plane direction (left panel in Figure 1b) in all samples with different molecular weights of P3HS (from 6K to 24K), suggesting that the chains in P3HS films were packed in an edge-on orientation manner. The P3HS-6K sample exhibited an intense (100) diffraction at q_z = 4.9 nm^{-1}, corresponding to an interlayer spacing between conjugated backbones (d_{100}, a-axis) of 12.8 Å (Figure 1c). As the molecular weight increases to 9K, another relatively weak diffraction at q_z = 3.8 nm^{-1} (d_{100} = 16.5 Å) also appeared (Figure 1d). The 12.8 and 16.5 Å diffraction peaks can be assigned to P3HS crystal form II and I, respectively.[25] These observations suggested that pure form II existed in P3HS-6K while form II and I coexisted in P3HS-9K. With the further increase in molecular weight, form I dominated in P3HS-11K (Figure 1e) while pure form I was obtained in P3HS-16K (Figure 1f) and P3HS-24K (Figure S3). Clearly, the results noted above demonstrated that lower molecular weight P3HS favored the formation of form II over form I crystalline structures, which is consistent with the previous reports on P3HS[25] and P3ATs.[30] This may be due largely to stronger interaction between side chains of adjacent P3HS that causes the side-chain interdigitation in the low molecular weight samples. Compared with the (010) diffraction along the in-plane direction (right panel in Figure 1b), the stacking period of P3HS backbones (d_{010}, b-axis) were 3.9 and 4.4 Å in form I and II, respectively, calculated from the scattering vectors $q_{x,y}$ of 16.0 and 14.3 nm^{-1}. This indicates that the lamellar stacking

DOI: 10.1021/acs.macromol.7b02126
Macromolecules 2017, 50, 9674–9682

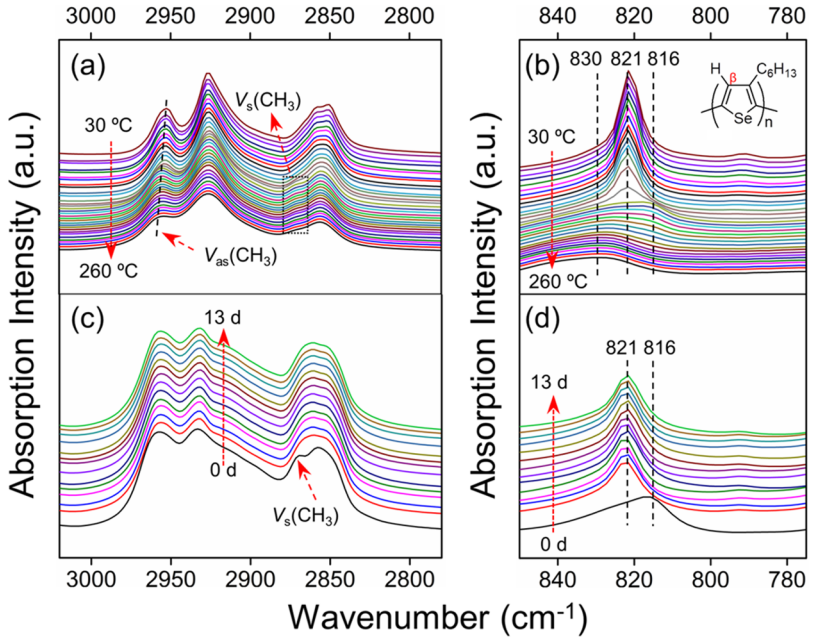

Figure 3. Temperature-dependent FTIR spectra of as-cast P3HS-6K film (with pure form II state to start with) in the (a) C−H stretching vibration region (3000−2800 cm^{-1}) and (b) C_β−H out-of-plane deformation band region (850−800 cm^{-1}) during the heating process from 30 to 260 °C, experiencing a form II to form I transition. The spectra were recorded at a 10 °C interval from 30 to 100 °C and from 180 to 260 °C and 5 °C interval from 100 to 180 °C. The dashed rectangle in (a) indicates the location of $\nu_s(CH_3)$. The inset in (b) illustrates the location of selenophene C_β. (c, d) FTIR spectral changes of the thermally annealed P3HS-6K film in (a) and (b) upon the subsequent THF vapor annealing treatment, undergoing a form I to form II transition.

along the *b*-axis is more closely packed in form I. On the basis of the above analysis, the structural models of P3HS with form I and II crystals can be depicted in Figure 1g.

Subsequently, P3HS-6K was chosen as a representative sample to investigate the phase transition between different crystalline polymorphs upon alternating thermal and solvent vapor annealing. Both thermal and solvent annealing have been widely used to influence the crystalline polymorphs of P3ATs and improve the ordering of their molecular packing.[31] Nonetheless, after thermal annealing of as-cast P3HS-6K film at 150 °C for 10 min, the initial pure form II crystals changed to form I completely (Figure 2a). Interestingly, the form I crystals reversed back to form II upon THF vapor annealing; however, such a transition occurred much slower (Figure 2b; approximately 9 days). This is not surprising as the polymer chains cannot move and reconstruct themselves until sufficient THF vapor penetrates into the P3HS-6K film and swells the polymer chains adequately. In addition to THF, chloroform and carbon disulfide were also tried as solvent for the vapor annealing. They also resulted in phase transition from form I to II. As the diffraction peak intensity is approximately proportional to the materials crystallinity, the 1D GIXRD profiles reduced along the out-of-plane direction indicated a much higher crystallinity in form I (thermally annealed) than form II (solvent vapor annealed) (Figure 2c). Notably, the phase transition from form I to II is highly reversible and can be repeated for several cycles prior to the occurrence of dewetting of the P3HS-6K film on the Si/SiO_2 substrate due partially to its low molecular weight. The driving force for such a phase transition between form I and II is the stability difference between these two crystalline polymorphs upon thermal or solvent vapor annealing. The transition from form I to II upon solvent vapor annealing and form II to I upon thermal annealing suggested that P3HS form I is thermodynamically stable form at the elevated temperature, while P3HS form II is a kinetically controlled form. Figure 2d depicts the reversible change in d_{100} spacing between 12.3 and 15.2 Å during a three-cycle phase transition where the *d* values were extracted from the X-ray diffraction (XRD) profiles using an as-cast P3HS-6K film (Figure S4). In addition to the reversible phase transition between two crystalline polymorphs (forms I and II) (Figure 2d), the P3HS-6K thin film also experienced a reversible morphological change from a more flat and less featured topology upon thermal annealing to a fibrillar network-like morphology upon solvent vapor annealing (Figure S5).

Since the phase transition from form I to II accomplished by THF vapor annealing was slow, the phase transition kinetics can be assessed by XRD (Figure 2e). To demonstrate the phase transition process more clearly, the peak intensity in each curve of Figure 2e was normalized. The thermally annealed P3HS-6K film showed the diffraction peaks at 2θ of 6.09°, 11.86°, and 17.64°, corresponding to the (100), (200), and (300) diffractions, respectively, of form I crystals. After exposure to THF vapor for 1 day, the (100) and (200) diffractions of form II crystals at 2θ of 7.53° and 14.79° emerged. With the prolonged THF vapor treatment, the diffraction intensity of form II crystals gradually exceeded that of form I. Finally, only the diffractions from form II crystals were observed after THF treatment for 9 days. The form I to II transition kinetics for P3HS films of different molecular weights were also compared by capitalizing on the $(100)_{II}/(100)_I$ intensity ratio ($I_{(100)II}/I_{(100)I}$) extracted from the respective XRD studies (Figure S6) to examine the phase transition rate (Figure 2f). Clearly, the $I_{(100)II}/I_{(100)I}$ increased with the extended solvent treatment in all P3HS films. The comparison of the slope *k* of different curves shows that the lowest molecular weight sample (i.e., P3HS-6K) displayed the fastest transition rate, and the rate decreased with the increased molecular weight up to 11K (inset

DOI: 10.1021/acs.macromol.7b02126
Macromolecules 2017, 50, 9674−9682

in Figure 2f). The P3HS-11K had the lowest transition rate, after which the rate increased with a further increase of molecular weight to 24 K.

There are three factors (i.e., chain length, chain packing mode, and film crystallinity) that greatly influenced the chain mobility and transition rate. After correction of the influence of the film thickness, the initial crystallinity of form I increased from P3HS-6K to P3HS-11K and then decreased from P3HS-11K to P3HS-24K (Figure S7). Such a trend is consistent with the previous report that the crystallinity of poly(3-butylthiophene) increased with molecular weight and then decreased with a further increase of molecular weight.[32] We note that it was reported that P3HT with the molecular weight below 10 kDa crystallized with the fully extended chains, while crystallized with the folded chains at the higher molecular weights.[33,34] P3HS is expected to exhibit a similar trend during crystallization with a higher turning point of molecular weight due to their similar molecular structure and more rigid polyselenophene backbone. At the lower molecular weights, P3HS-6K, -9K, and -11K crystallized in the extended chains. P3HS-11K has a higher molecular weight with a longer conjugation length and stronger intermolecular $\pi-\pi$ interactions than P3HS-6K and -9K, thereby resulting in a more ordered packing of crystals. In addition, when the molecular weight is low, the end groups of P3HS chains can be regarded as the impurity and P3HS-6K with the lowest molecular weight has the highest content of impurity, which decreased the crystallinity. At the higher molecular weights, P3HS-16K and -24K crystallized in the folded chains which involved a periodic alternation of crystalline lamellae separated by amorphous interlamellar zones,[34] thus decreasing their crystallinity. Moreover, the chain entanglement and decreased solubility of P3HS at the higher molecular weights may also hinder the formation of more ordered regions. It is known that the RR affects the crystallization of conjugated polymers. Since the RR of all the P3HS samples used is high (95%−96%) and very close (Table S1), such small variation in RR would not cause the difference in the crystallinity of each sample. Overall, P3HS with shorter and extended chains have higher chain mobility upon THF vapor annealing compared to the longer and folded chains. In addition, the P3HS samples with lower crystallinity can be readily destroyed by the THF vapor and transformed into form II. Thus, the synergy of high chain mobility and low crystallinity resulted in the fastest transition rate in P3HS-6K. P3HS-11K form I crystals with the highest crystallinity showed the slowest transition rate from form I to II (i.e., smallest k in the inset of Figure 2f). We note that after the transformation into form II, the prolonged THF treatment led to the reduced $I_{(100)II}$ owing to the dewetting and fractures of polymer films (Figure S8). Consequently, the $I_{(100)II}/I_{(100)I}$ dropped considerably (data not shown here).

In order to elucidate the molecular structure changes during the phase transition process, infrared spectroscopy (FTIR) measurements, which are sensitive to chain conformation of semicrystalline polymers, were performed. Figure 3 shows the FTIR spectral changes of as-cast P3HS-6K film upon heating from 30 to 260 °C (i.e., experiencing a form II to form I transition) (Figure 3a,b), followed by subsequent THF vapor treatment (i.e., undergoing a transition recovery from form I to form II) (Figure 3c,d). Most of the FTIR characteristic bands of P3HT have been well established, including the C−H stretching vibration bands in the 3000−2800 cm^{-1} region associated with the alkyl side chain,and the out-of-plane deformation modes of thiophene C_β−H in the 850−800 cm^{-1} region attributed to the $\pi-\pi$ stacking of the planar backbones.[35,36] The classification of these regions should also be applicable to P3HS due to their similar molecular structure. In our study, the assignments of the characteristic bands for P3HS are summarized in Table S2. As evidenced in Figure 3a, for the bands in the 3000−2800 cm^{-1} region, the $\nu_s(CH_3)$ located around 2873 cm^{-1} started to appear at 120−135 °C, and the $\nu_{as}(CH_3)$ at 2952 cm^{-1} shifted to a higher frequency (2959 cm^{-1}) in this temperature range, implying the disordering of the end CH_3 packing of the hexyl side chain.[36] This is because at the initial stage of form II the $\nu_s(CH_3)$ was undetectable due to the interdigitation of hexyl side chains (right panel in Figure 1g). After thermal annealing at 120−135 °C, the form II crystals began to transform to form I, and the overlapping of hexyl side chains became minimal, leading to the appearance of $\nu_s(CH_3)$. Figure 3b shows temperature-dependent FTIR spectral changes of selenophene C_β−H out-of-plane deformation modes in the 850−800 cm^{-1} region. As noted above, the selenophene C_β−H is attached directly to the conjugated ring, and its vibration is along the $\pi-\pi$ stacking direction (inset in Figure 3b). Notably, three bands located at 821, 816, and 830 cm^{-1} sequentially dominated as the temperature increased. The intensity of 821 cm^{-1} band decreased and red-shifted to 816 cm^{-1} at 120−135 °C. In conjunction with the GIXRD and XRD results (Figures 1 and 2), the bands at 821 and 816 cm^{-1} can be assigned to the form II and I crystals of P3HS, respectively. In the melting temperature range (the melting temperature of P3HS-6K is ∼180 °C), an amorphous halo with a peak centered at 830 cm^{-1} was observed. The band shift from 821 to 816 cm^{-1} of the $\delta(C_\beta-H)$ suggests the decreased interchain $\pi-\pi$ interaction strength during the form II to I transition,[36] which appears to be inconsistent with the decreased d_{010} from form II (d_{010} = 4.4 Å) to form I (d_{010} = 3.9 Å) extracted from the 1D in-plane direction in GIXRD measurements (Figure 1b,g). According to the tilted stacking model of P3HT, the interplanar $\pi-\pi$ stacking distance ($d_{\pi-\pi}$) is shorter than the stacking period of backbones along the b-axis (d_{010}). Their relationship can be expressed as $d_{\pi-\pi} = d_{010} \cos\theta$, where θ is the angle between the $\pi-\pi$ stacking direction and the b-axis.[36−38] Figure 1g illustrates the tilted stacking model of form II crystals of P3HS in our work, which explains the seeming discrepancy between FTIR and GIXRD results. The decreased $\pi-\pi$ interaction strength from form II to I revealed by FTIR, that is, the increased $d_{\pi-\pi}$ spacing, may come from the decreased tilting angle θ during the form II to I transition.

For the reversed transition from form I obtained after thermal annealing to form II upon the subsequent solvent treatment, both the disappearance of $\nu_s(CH_3)$ band around 2873 cm^{-1} (Figure 3c) and blue-shift of C_β−H out-of-plane deformation mode from 816 to 821 cm^{-1} (Figure 3d) occurred only after 1 day and remained unchanged during the following 12 days. Thus, it is plausible that the phase transition from form I to II may complete after 1 day, which was not consistent with the XRD results where it took 9 days to achieve the phase transition (Figure 2e). This inconsistence may be rationalized as follows. The utility of FTIR stems from its specificity to different molecular groups[35] and the two bands at 2873 and 816 cm^{-1} are conformation-sensitive. In contrast, XRD characterizes the crystalline structures in a much larger scale. Therefore, less time is taken to change the P3HS chain conformation (FTIR), and however longer time is needed to

DOI: 10.1021/acs.macromol.7b02126
Macromolecules 2017, 50, 9674−9682

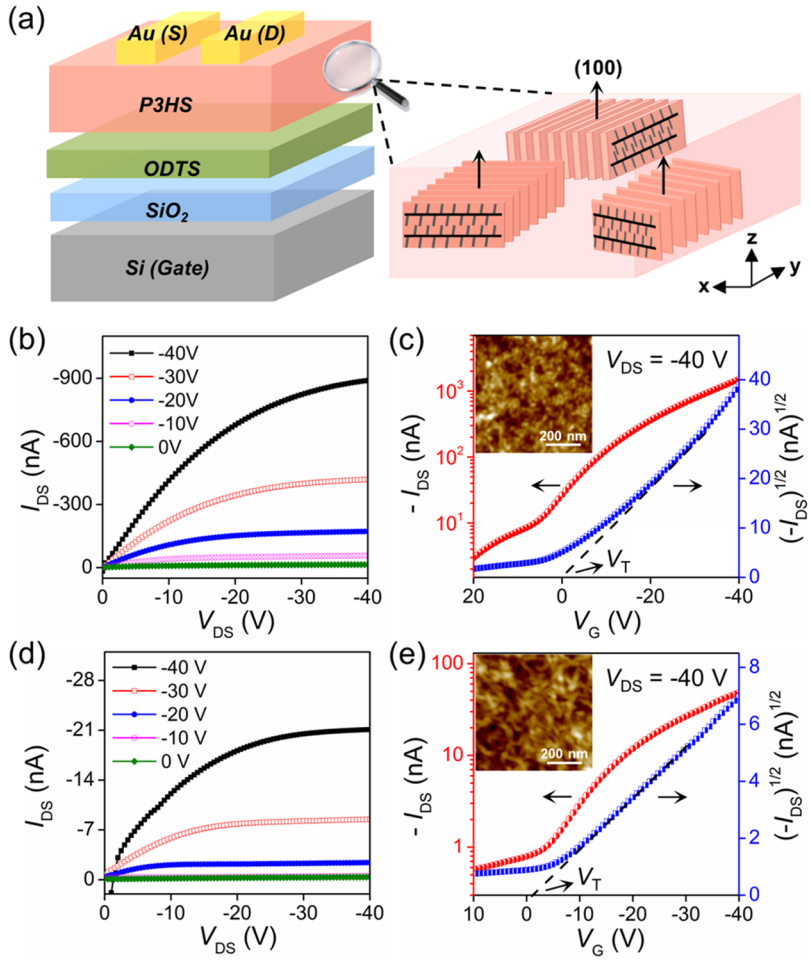

Figure 4. (a) Schematic illustration of OFET device structure with a top-contact bottom-gate configuration used in the measurement. The arrows indicate the (100) directions of P3HS crystals. (b, d) Output and (c, e) transfer curves of OFETs fabricated with (b, c) P3HS-11K form I film and (d, e) P3HS-11K form II film. V_{DS} = −40 V. From the intercept with *x*-axis (i.e., V_G axis), the threshold voltage V_T can be obtained as marked in (c) and (e). The insets in (c) and (e) are the corresponding AFM images.

Table 1. Summary of Hole Transport Properties of P3HS Films with Varied Molecular Weights and Different Crystalline Polymorphs

samples	polymorphs	μ_{max} [a] ($cm^2\ V^{-1}\ s^{-1}$)	μ_{avg} [b] ($cm^2\ V^{-1}\ s^{-1}$)	I_{on}/I_{off} [c]	V_{th} [d] (V)
P3HS-6K	form I	8.067×10^{-4}	4.942×10^{-4}	$>10^3$	−10.0
	form II	1.598×10^{-4}	1.266×10^{-4}	$>10^3$	−2.0
P3HS-9K	form I	3.792×10^{-3}	3.375×10^{-3}	$>10^4$	−12.0
	form II	3.909×10^{-4}	3.605×10^{-4}	$>10^3$	−5.0
P3HS-11K	form I	1.743×10^{-2}	1.567×10^{-2}	$>10^5$	−9.0
	form II	2.011×10^{-3}	1.846×10^{-3}	$>10^4$	−5.0
P3HS-16K	form I	4.081×10^{-3}	2.976×10^{-3}	$>10^4$	−15.0
	form II	5.912×10^{-4}	4.986×10^{-4}	$>10^4$	−10.0
P3HS-24K	form I	4.099×10^{-4}	2.563×10^{-4}	$>10^4$	−10.0
	form II	9.299×10^{-5}	7.905×10^{-5}	$>10^3$	−6.0

[a]Maximum charge carrier mobility. [b]Average charge carrier mobility obtained from at least six OFET devices. [c]Current on/off ratio. [d]Threshold voltage.

accomplish the chain packing (XRD) during the form I to II transition.

The ability to understand the correlation between the crystalline polymorphs (i.e., forms I and II) of P3HS and charge transport properties will facilitate the development of P3HS-based thin-film transistors. To this end, bottom-gate top-contact OFET devices based on P3HS were fabricated (Figure 4a). As a representative example, the output and transfer curves of P3HS-11K film with form I and II crystals are shown in Figure 4b−e. We note that the output and transfer profiles of OFETs prepared from all the P3HS samples suggested typical p-type semiconductor characteristics with well-resolved linear current regimes (Ohmic region) at low drain voltages, signfying that hole carrier injection from the Au source to the P3HS film was efficient.[39] The field-effect mobility (μ_{FET}) was calculated

DOI: 10.1021/acs.macromol.7b02126
Macromolecules 2017, 50, 9674−9682

from the transfer curves in the saturation regime (V_{DS} = −40 V) according to the following equation:[40]

$$I_{DS} = \frac{W}{2L}\mu_{FET}C_g(V_G - V_T)^2$$

where I_{DS} is the drain current, C_g is the capacitance of the gate dielectric, V_G is the gate-source voltage, V_T is the threshold voltage, and W (300 μm) and L (30 μm) are the width and length of the transistor channel, respectively. The resulting mobilities of P3HS films with different molecular weights and crystalline polymorphs are summarized in Table 1. In all cases, the highest mobility as well as the average mobility was obtained by measuring at least six transistors. As noted above, P3HS films with form I and II crystals adopt the edge-on orientation, which is favorable for achieving high carrier mobility as the direction of $\pi-\pi$ stacking is in the plane of the current-flow direction (close-up in Figure 4a). The differences between form I and II of P3HS are the interlayer spacing between conjugated backbones, $\pi-\pi$ stacking distance, crystallinity, thin film microstructure, etc. Compared to the charge carrier mobilities of different P3HS samples (Table 1), the crystallinity was found to play a primary role in the charge transport performance of thin film. The mobility of form I with higher crystallinity was approximately 1 order of magnitude higher than that of form II in P3HS films of different molecular weights. This is not surprising as the charge carriers typically move faster in crystalline region than in amorphous region. The highest carrier mobility of 1.74×10^{-2} cm^2 V^{-1} s^{-1} was seen in the P3HS-11K film with form I crystals as it possessed the highest crystallinity and the lowest PDI (Figure S7 and Table S1). This value was comparable to the charge mobilities (0.02−0.04 cm^2 V^{-1} s^{-1}) of P3HS with the molecular weights in the range of 70−200 kDa and a PDI of 2.[27] The AFM images in the inset of Figure 4c,e show that the form I of P3HS-11K had smoother and smaller domain size than form II (the root-mean-square roughness in form I and II is 1.30 and 5.36 nm, respectively). We hypothesize that the smoother morphology (form I) is likely to promote the connectivity between the ordered crystalline regions for effective charge transport, while the presence of more grain boundaries in form II negatively impacted the charge carrier mobility. It is notable that large single crystals of P3HT form II were prepared via a self-seeding approach, which are good model systems to be used to explore the charge transport as a function of molecular orientation within the crystals.[41] It is expected that if single crystals of P3HS form II are prepared by this approach, they likely have higher charge mobilities than polycrystalline form II. When comparing the film morphology of P3HS with different molecular weights, it is clear that the rod-like crystals of P3HS film with lower molecular weights (6K and 9K) had more grain boundaries than that of isotropic nodules of the high molecular weight films (11K, 16K, and 24K) (Figure S9). Taken together, the highest crystallinity, the lowest PDI, optimal chain length, and good film morphology are supportive of the highest charge mobility of P3HS-11K over other P3HS films in our study. For P3HS-16K and P3HS-24K, in spite of longer chain length and smooth morphology, their crystallinities were much lower than P3HS-11K, thus leading to lower charge mobilities.

CONCLUSION

In summary, we studied the crystallization and phase transition between form I and II of P3HS films with different molecular weights. Interestingly, the phase transition is highly reversible and can be readily enabled by alternating thermal and solvent vapor annealing treatments. Among all P3HS studied, pure form II crystals existed in as-cast P3HS-6K film, while pure form I crystals produced in as-cast P3HS-16K and P3HS-24K films. Thermal annealing transformed as-cast P3HS-6K film with pure form II crystals into form I. The transition kinetics (from as-cast form II to thermally annealed form I) was found to be much faster than the reverse transition (from thermally annealed form I to form II rendered by subsequent solvent annealing). The phase transition and its kinetics were thoroughly investigated by a suite of techniques (GIXRD, XRD, FTIR, and AFM). In particular, the molecular structure changes during the phase transition was revealed by the detailed temperature-dependent FTIR studies. More importantly, the correlation between crystalline structures (form I and II) with field-effect mobility was explored for the first time. The P3HS-11K film with form I crystals demonstrated the best OFET performance with a charge mobility of 1.74×10^{-2} cm^2 V^{-1} s^{-1}. Further improvement of charge mobility is expected, as many device parameters have not yet been optimized. Nonetheless, the fundamental understanding on crystallization and phase transition of P3HS films gained from this work may enable the development of polyselenophene-based materials and devices for use in OFETs, LEDs, solar cells, optical imaging, and sensors.

ASSOCIATED CONTENT

Supporting Information

The Supporting Information is available free of charge on the ACS Publications website at DOI: 10.1021/acs.macromol.7b02126.

Detail synthesis of P3HS and their molecular weights, FTIR bands of P3HS, GIXRD image of as-cast P3HS-24K film, XRD images of P3HS-6K, -9K, -11K, -16K, and -24K form I and II films, FESEM images of as-cast P3HS-6K film and after thermal and THF vapor annealing, crystallinities of P3HS form I films with different molecular weights, AFM images of P3HS films with different molecular weights and crystalline polymorphs (PDF)

AUTHOR INFORMATION

Corresponding Authors

*E-mail: juanpeng@fudan.edu.cn (J.P.).
*E-mail: zhiqun.lin@mse.gatech.edu (Z.L.).

ORCID

Zhiqun Lin: 0000-0003-3158-9340

Notes

The authors declare no competing financial interest.

ACKNOWLEDGMENTS

This work was financially supported by the National Natural Science Foundation of China (Grants 21674024 and 21320102005) and Ministry of Science and Technology of China (2016YFA0203301). Z.L. acknowledges the Senior Visiting Scholarship of State Key Laboratory, Fudan University (17FGJ07). The authors also thank Dr. X. Chen for helpful discussions on OFET. We gratefully acknowledge the support from Shanghai Synchrotron Radiation Facility of China for using the BL14B1 and BL16B1 beamlines.

DOI: 10.1021/acs.macromol.7b02126
Macromolecules 2017, 50, 9674−9682

REFERENCES

(1) Salleo, A. Charge Transport in Polymeric Transistors. *Mater. Today* **2007**, *10*, 38−45.
(2) Wang, C.; Dong, H.; Hu, W.; Liu, Y.; Zhu, D. Semiconducting π-Conjugated Systems in Field-Effect Transistors: A Material Odyssey of Organic Electronics. *Chem. Rev.* **2012**, *112*, 2208−2267.
(3) Pan, S.; He, L.; Peng, J.; Qiu, F.; Lin, Z. Chemical-Bonding-Directed Hierarchical Assembly of Nanoribbon-Shaped Nanocomposites of Gold Nanorods and Poly(3-hexylthiophene). *Angew. Chem., Int. Ed.* **2016**, *55*, 8686−8690.
(4) He, M.; Han, W.; Ge, J.; Yang, Y.; Qiu, F.; Lin, Z. All-conjugated Poly(3-alkylthiophene) Diblock Copolymer Based Bulk Heterojunction Solar Cells with Controlled Molecular Organization and Nanoscale Morphology. *Energy Environ. Sci.* **2011**, *4*, 2894−2902.
(5) Han, W.; He, M.; Byun, M.; Li, B.; Lin, Z. Large-scale Hierarchically Structured Conjugated Polymer Assemblies with Enhanced Electrical Conductivity. *Angew. Chem., Int. Ed.* **2013**, *52*, 2564−2568.
(6) Chang, M.; Choi, D.; Fu, B.; Reichmanis, E. Solvent Based Hydrogen Bonding: Impact on Poly(3-hexylthiophene) Nanoscale Morphology and Charge Transport Characteristics. *ACS Nano* **2013**, *7*, 5402−5413.
(7) Kim, S. H.; Jang, M.; Yang, H.; Anthony, J. E.; Park, C. E. Organic Field-Effect Transistors: Physicochemically Stable Polymer-Coupled Oxide Dielectrics for Multipurpose Organic Electronic Applications. *Adv. Funct. Mater.* **2011**, *21*, 2198−2207.
(8) Aiyar, A. R.; Hong, J.; Reichmanis, E. Regioregularity and Intrachain Ordering: Impact on the Nanostructure and Charge Transport in Two-Dimensional Assemblies of Poly(3-hexylthiophene). *Chem. Mater.* **2012**, *24*, 2845−2853.
(9) Chu, P. H.; Wang, G.; Fu, B.; Choi, D.; Park, J. O.; Srinivasarao, M.; Reichmanis, E. Synergistic Effect of Regioregular and Regiorandom Poly(3-hexylthiophene) Blends for High Performance Flexible Organic Field Effect Transistors. *Adv. Electron. Mater.* **2016**, *2*, 1500384.
(10) Lee, Y.; Oh, J. Y.; Son, S. Y.; Park, T.; Jeong, U. Effects of Regioregularity and Molecular Weight on the Growth of Polythiophene Nanofibrils, and Mixes of Short and Long Nanofibrils to Enhance the Hole Transport. *ACS Appl. Mater. Interfaces* **2015**, *7*, 27694−27702.
(11) Kline, R. J.; McGehee, M. D.; Kadnikova, E. N.; Liu, J.; Fréchet, J. M. J. Controlling the Field-Effect Mobility of Regioregular Polythiophene by Changing the Molecular Weight. *Adv. Mater.* **2003**, *15*, 1519−1522.
(12) He, M.; Zhao, L.; Wang, J.; Han, W.; Yang, Y.; Qiu, F.; Lin, Z. Self-Assembly of All-Conjugated Poly(3-alkylthiophene) Diblock Copolymer Nanostructures from Mixed Selective Solvents. *ACS Nano* **2010**, *4*, 3241−3247.
(13) Yang, H.; Shin, T. J.; Yang, L.; Cho, K.; Ryu, C. Y.; Bao, Z. Effect of Mesoscale Crystalline Structure on the Field-Effect Mobility of Regioregular Poly(3-hexylthiohene) in Thin-Film Transistors. *Adv. Funct. Mater.* **2005**, *15*, 671−676.
(14) Park, Y. D.; Lee, S. G.; Lee, H. S.; Kwak, D.; Lee, D. H.; Cho, K. Solubility-Driven Polythiophene Nanowires and Their Electrical Characteristics. *J. Mater. Chem.* **2011**, *21*, 2338−2343.
(15) Skrypnychuk, V.; Wetzelaer, G. A. H.; Gordiichuk, P. I.; Mannsfeld, S. C. B.; Herrmann, A.; Toney, M. F.; Barbero, D. R. Ultrahigh Mobility in an Organic Semiconductor by Vertical Chain Alignment. *Adv. Mater.* **2016**, *28*, 2359−2366.
(16) Ye, Z.; Yang, X.; Cui, H.; Qiu, F. Nanowires with Unusual Packing of Poly(3-hexylthiophene)s Induced by Electric Fields. *J. Mater. Chem. C* **2014**, *2*, 6773−6780.
(17) Salammal, S. T.; Mikayelyan, E.; Grigorian, S.; Pietsch, U.; Koenen, N.; Scherf, U.; Kayunkid, N.; Brinkmann, M. Impact of Thermal Annealing on the Semicrystalline Nanomorphology of Spin-Coated Thin Films of Regioregular Poly(3-alkylthiophene)s as Observed by High-Resolution Transmission Electron Microscopy and Grazing Incidence X-ray Diffraction. *Macromolecules* **2012**, *45*, 5575−5585.
(18) Lu, G.; Li, L.; Yang, X. Achieving Perpendicular Alignment of Rigid Polythiophene Backbones to the Substrate by Using Solvent-Vapor Treatment. *Adv. Mater.* **2007**, *19*, 3594−3598.
(19) Wijsboom, Y. H.; Patra, A.; Zade, S. S.; Sheynin, Y.; Li, M.; Shimon, L. J. W.; Bendikov, M. Controlling Rigidity and Planarity in Conjugated Polymers: Poly(3,4-ethylenedithioselenophene). *Angew. Chem., Int. Ed.* **2009**, *48*, 5443−5447.
(20) Ballantyne, A. M.; Chen, L.; Nelson, J.; Bradley, D. D. C.; Astuti, Y.; Maurano, A.; Shuttle, C. G.; Durrant, J. R.; Heeney, M.; Duffy, W.; McCulloch, I. Studies of Highly Regioregular Poly(3-hexylselenophene) for Photovoltaic Applications. *Adv. Mater.* **2007**, *19*, 4544−4547.
(21) Khim, D.; Lee, W. H.; Baeg, K. J.; Kim, D. Y.; Kang, I. N.; Noh, Y. Y. Highly Stable Printed Polymer Field-Effect Transistors and Inverters via Polyselenophene Conjugated Polymers. *J. Mater. Chem.* **2012**, *22*, 12774−12783.
(22) Poverenov, E.; Sheynin, Y.; Zamoshchik, N.; Patra, A.; Leitus, G.; Perepichka, I. F.; Bendikov, M. Flat Conjugated Polymers Combining a Relatively Low HOMO Energy Level and Band Gap: Polyselenophenes Versus Polythiophenes. *J. Mater. Chem.* **2012**, *22*, 14645−14655.
(23) Chen, Z.; Lemke, H.; Albert-Seifried, S.; Caironi, M.; Nielsen, M. M.; Heeney, M.; Zhang, W.; McCulloch, I.; Sirringhaus, H. High Mobility Ambipolar Charge Transport in Polyselenophene Conjugated Polymers. *Adv. Mater.* **2010**, *22*, 2371−2375.
(24) Patra, A.; Bendikov, M. Polyselenophenes. *J. Mater. Chem.* **2010**, *20*, 422−433.
(25) Li, L.; Hollinger, J.; Jahnke, A. A.; Petrov, S.; Seferos, D. S. Polyselenophenes with Distinct Crystallization Properties. *Chem. Sci.* **2011**, *2*, 2306−2310.
(26) Wang, Y.; Liu, X.; Peng, J.; Qiu, F. Controlling Morphology and Crystalline Structure in Poly(3-hexylselenophene) Solutions During Aging. *RSC Adv.* **2015**, *5*, 107970−107976.
(27) Heeney, M.; Zhang, W.; Crouch, D. J.; Chabinyc, M. L.; Gordeyev, S.; Hamilton, R.; Higgins, S. J.; McCulloch, I.; Skabara, P. J.; Sparrowe, D.; Tierney, S. Regioregular Poly(3-hexyl)selenophene: A Low Band Gap Organic Hole Transporting Polymer. *Chem. Commun.* **2007**, 5061−5063.
(28) Yokoyama, A.; Miyakoshi, R.; Yokozawa, T. Chain-Growth Polymerization for Poly(3-hexylthiophene) with a Defined Molecular Weight and a Low Polydispersity. *Macromolecules* **2004**, *37*, 1169−1171.
(29) Loewe, R. S.; Ewbank, P. C.; Liu, J.; Zhai, L.; McCullough, R. D. Regioregular, Head-to-Tail Coupled Poly(3-alkylthiophenes) Made Easy by the GRIM Method: Investigation of the Reaction and the Origin of Regioselectivity. *Macromolecules* **2001**, *34*, 4324−4333.
(30) Meille, S. V.; Romita, V.; Caronna, T.; Lovinger, A. J.; Catellani, M.; Belobrzeckaja, L. Influence of Molecular Weight and Regioregularity on the Polymorphic Behavior of Poly(3-decylthiophenes). *Macromolecules* **1997**, *30*, 7898−7905.
(31) Lu, G.; Li, L.; Yang, X. Morphology and Crystalline Transition of Poly(3-butylthiophene) Associated with Its Polymorphic Modifications. *Macromolecules* **2008**, *41*, 2062−2070.
(32) Li, S.; Wang, S.; Zhang, B.; Ye, F.; Tang, H.; Chen, Z.; Yang, X. Synergism of Molecular Weight, Crystallization and Morphology of Poly(3-butylthiophene) for Photovoltaic Applications. *Org. Electron.* **2014**, *15*, 414−427.
(33) Liu, J.; Arif, M.; Zou, J.; Khondaker, S. I.; Zhai, L. Controlling Poly(3-hexylthiophene) Crystal Dimension: Nanowhiskers and Nanoribbons. *Macromolecules* **2009**, *42*, 9390−9393.
(34) Brinkmann, M.; Rannou, P. Effect of Molecular Weight on the Structure and Morphology of Oriented Thin Films of Regioregular Poly(3-hexylthiophene) Grown by Directional Epitaxial Solidification. *Adv. Funct. Mater.* **2007**, *17*, 101−108.
(35) Yuan, Y.; Zhang, J.; Sun, J. Effect of Solvent Evaporation Rate on Order-to-Disorder Phase Transition Behavior of Regioregular Poly(3-butylthiophene). *Macromolecules* **2011**, *44*, 6128−6135.
(36) Yuan, Y.; Zhang, J.; Sun, J.; Hu, J.; Zhang, T.; Duan, Y. Polymorphism and Structural Transition Around 54 °C in

DOI: 10.1021/acs.macromol.7b02126
Macromolecules 2017, 50, 9674−9682

Regioregular Poly(3-hexylthiophene) with High Crystallinity As Revealed by Infrared Spectroscopy. *Macromolecules* **2011**, *44*, 9341−9350.
(37) Buono, A.; Son, N. H.; Raos, G.; Gila, L.; Cominetti, A.; Catellani, M.; Meille, S. V. Form II Poly(3-butylthiophene): Crystal Structure and Preferred Orientation in Spherulitic Thin Films. *Macromolecules* **2010**, *43*, 6772−6781.
(38) Kayunkid, N.; Uttiya, S.; Brinkmann, M. Structural Model of Regioregular Poly(3-hexylthiophene) Obtained by Electron Diffraction Analysis. *Macromolecules* **2010**, *43*, 4961−4967.
(39) Kwak, D.; Choi, H. H.; Kang, B.; Kim, D. H.; Lee, W. H.; Cho, K. Tailoring Morphology and Structure of Inkjet-Printed Liquid-Crystalline Semiconductor/Insulating Polymer Blends for High-Stability Organic Transistors. *Adv. Funct. Mater.* **2016**, *26*, 3003−3011.
(40) Na, J. Y.; Kang, B.; Sin, D. H.; Cho, K.; Park, Y. D. Understanding Solidification of Polythiohene Thin Films During Spin-Coating: Effects of Spin-Coating Time and Processing Additives. *Sci. Rep.* **2015**, *5*, 13288.
(41) Rahimi, K.; Botiz, I.; Stingelin, N.; Kayunkid, N.; Sommer, M.; Koch, F. P. V.; Nguyen, H.; Coulembier, O.; Dubois, P.; Brinkmann, M.; Reiter, G. Controllable Processes for Generating Large Single Crystals of Poly(3-hexylthiophene). *Angew. Chem., Int. Ed.* **2012**, *51*, 11131−11135.

DOI: 10.1021/acs.macromol.7b02126
Macromolecules 2017, 50, 9674−9682